frontiers in Astronomy and Space Sciences

ORIGINAL RESEARCH
published: 23 March 2022
doi: 10.3389/fspas.2022.836811

Storm-Time Evolution of the Equatorial Electron Pitch Angle Distributions in Earth's Outer Radiation Belt

Artem Smirnov[1,2]*, *Yuri Shprits*[1,2,3], *Hayley Allison*[1], *Nikita Aseev*[1], *Alexander Drozdov*[3], *Peter Kollmann*[4], *Dedong Wang*[1] *and Anthony A. Saikin*[3]

[1]Helmholtz Centre Potsdam - GFZ German Research Centre for Geosciences, Potsdam, Germany, [2]Institute of Physics and Astronomy, University of Potsdam, Potsdam, Germany, [3]Department of Earth, Planetary and Space Sciences, University of California, Los Angeles, Los Angeles, CA, United States, [4]Applied Physics Laboratory, Johns Hopkins University, Laurel, MD, United States

In this study we analyze the storm-time evolution of equatorial electron pitch angle distributions (PADs) in the outer radiation belt region using observations from the Magnetic Electron Ion Spectrometer (MagEIS) instrument aboard the Van Allen Probes in 2012–2019. The PADs are approximated using a sum of the first, third and fifth sine harmonics. Different combinations of the respective coefficients refer to the main PAD shapes within the outer radiation belt, namely the pancake, flat-top, butterfly and cap PADs. We conduct a superposed epoch analysis of 129 geomagnetic storms and analyze the PAD evolution for day and night MLT sectors. PAD shapes exhibit a strong energy-dependent response. At energies of tens of keV, the PADs exhibit little variation throughout geomagnetic storms. Cap PADs are mainly observed at energies < 300 keV, and their extent in L shrinks with increasing energy. The cap distributions transform into the pancake PADs around the main phase of the storm on the nightside, and then come back to their original shapes during the recovery phase. At higher energies on the dayside, the PADs are mainly pancake during pre-storm conditions and become more anisotropic during the main phase. The quiet-time butterfly PADs can be observed on the nightside at $L > 5.6$. During the main phase, butterfly PADs have stronger 90°-minima and can be observed at lower L-shells (down to $L = 5$), then transitioning into flat-top PADs at $L \sim 4.5 - 5$ and pancake PADs at $L < 4.5$. The resulting PAD coefficients for different energies, locations and storm epochs can be used to test the wave models and physics-based radiation belt codes in terms of pitch angle distributions.

Keywords: pitch angle, pitch angle distributions, electrons, radiation belts, magnetosphere, van allen probes

OPEN ACCESS

Edited by:
Olga V. Khabarova, Institute of Terrestrial Magnetism Ionosphere and Radio Wave Propagation (RAS), Russia

Reviewed by:
Nickolay Ivchenko, Royal Institute of Technology, Sweden
Qiugang Zong, Peking University, China

***Correspondence:**
Artem Smirnov
artem.smirnov@gfz-potsdam.de

Specialty section:
This article was submitted to Space Physics, a section of the journal Frontiers in Astronomy and Space Sciences

Received: *15 December 2021*
Accepted: *01 March 2022*
Published: *23 March 2022*

Citation:
Smirnov A, Shprits Y, Allison H, Aseev N, Drozdov A, Kollmann P, Wang D and Saikin AA (2022) Storm-Time Evolution of the Equatorial Electron Pitch Angle Distributions in Earth's Outer Radiation Belt. Front. Astron. Space Sci. 9:836811. doi: 10.3389/fspas.2022.836811

1 INTRODUCTION

The radiation belts of the Earth contain charged energetic particles, mainly electrons and protons, trapped by the geomagnetic field. The energetic electrons are primarily observed in two regions, namely the inner ($L < 2.5$) and outer ($3.5 < L < 7$) belts, separated by the slot region where fluxes typically drop by several orders of magnitude (e.g., Ganushkina et al., 2011). The radiation belt electrons can be characterized in terms of their flux intensity and angular distributions (e.g., Clark

et al., 2014). These distributions, also named the pitch angle distributions (PADs), play a crucial role in understanding the dynamics of the radiation belts, as specific PAD types can reveal the processes governing the particle transport, source and loss mechanisms, and wave activities (e.g., Horne et al., 2003; Gannon et al., 2007; Ni et al., 2015).

There are several common types of pitch angle distributions in the radiation belt region. The so-called pancake, or normal, PADs have a maximum flux at 90° pitch angle (PA) with a smooth decrease in flux towards the loss cone (e.g., West et al., 1973). The pancake PADs can be formed as a result of the particle PA diffusion, inward radial diffusion, as well as wave-particle interactions (e.g., with hiss and chorus waves in the outer belt (Su et al., 2009; Meredith et al., 2000)), and consititute the most dominant PAD type in the inner magnetosphere on the dayside (Gannon et al., 2007). The PADs where electron flux at 90° is smaller than at intermediate pitch angles (~ 30°–75°) are called the butterfly distributions (West et al., 1973). The butterfly PADs in the outer radiation belt are mainly present at nightside magnetic local times (MLTs) and form due to drift shell splitting (Roederer, 1967; Sibeck et al., 1987), magnetopause shadowing (West et al., 1973) and wave activity (Artemyev et al., 2015; Ni et al., 2020). The flat-top PADs exhibit a relatively constant flux at a wide range of pitch angles around 90°. The flat-top PADs can be a transition phase between the butterfly and pancake PADs, and they also occur due to strong wave-particle interactions with whistler mode waves in regions of low electron densities (Horne et al., 2003). The head-and-shoulders, or cap, distributions resemble pancake PADs for non-equatorially mirroring electrons but have an additional bump in flux around 90° PA; they generally result from resonant interactions with the plasmaspheric hiss waves (Lyons et al., 1972). Wave-particle interactions with ultra low frequency (ULF) waves, particularly in the Pc4-Pc5 range, are known to also affect the electron pitch angle distributions (Zong et al., 2017). For instance, during the drift resonance events electron flux oscillations around 90° are observed faster than at lower PAs, which leads to the formation of the so-called boomerang stripes in the pitch angle distributions (e.g., Hao et al., 2017; Zhao et al., 2020).

Pitch angle distributions can be approximated using different trigonometric functions. The standard formulation used in several previous studies includes fitting PADs to the $\sin^n\alpha$, where α is the particle pitch angle and n is the steepness of the distribution (see e.g., Vampola, 1998; Gannon et al., 2007, etc.). This parametrisation, however, has several limitations. For instance, it fails to capture butterfly distributions which constitute the dominant PAD shape on the nightside at L > 5, as well as cap distributions occurring at lower L-shells (e.g., Zhao et al., 2018; Allison et al. (2018)). To mitigate this limitation, Allison et al. (2018) employed a combination of two terms of the said form, which allowed to resolve the cap distributions. Another formulation used in the radiation belts research includes fitting equatorial PADs with Legendre polynomials which comprise a set of spherical functions (see e.g., Chen et al., 2014; Zhao et al., 2018; Zhao et al., 2021). In particular, Zhao et al. (2018) demonstrated that equatorial PADs in the outer zone can be approximated by the first 3 even terms of the Legendre series expansion, while at L < 3 it was necessary to include higher harmonics due to the larger loss cones and generally steeper PAD shapes. In this study, we use Fourier sine series expansion to approximate equatorial electron PADs (**Eq. 1**). The Fourier expansion has been used for PAD approximation in the planetary magnetospheres (for Saturn's radiation belts Clark et al., 2014) but to our knowledge has not been applied to study electrons in the Earth's radiation belts yet. One of the main advantages of using the Fourier sine series expansion is a possibility to integrate **Equation 1** over the solid angle to derive omnidirectional flux.

Several studies have investigated the morphology of electron pitch angle distributions in the inner magnetosphere, both during quiet and geomagnetically active times. Roederer (1967) analyzed effects of the drift shell splitting on energetic electrons in the model magnetosphere and demonstrated that the drift shell splitting effects could only be observed above L = 5. The spatial structure of 80 keV–2.8 MeV electron PADs was described by West et al. (1973) using Ogo-5 satellite data. The dayside PADs were found to exhibit mainly pancake shape, while the nightside distributions at L > ~ 6 showed butterfly shapes, which were attributed to a combination of the drift shell splitting in presence of a negative flux gradient in L, and magnetopause shadowing. Selesnick and Blake (2002) computed anisotropies of relativistic electron PADs by tracing drift paths of particles for different pitch angles and levels of Kp and found a good agreement with average flux anisotropies calculated from Polar electron data under quiet geomagnetic conditions. Lyons et al. (1972) was one of the first papers that computed the PA-diffusion of electrons at energies 20 keV–2 MeV driven by the resonant interactions with whisler mode waves and showed the existence of the cap pitch angle distributions could be attributed to the resonant interactions with the plasmaspheric hiss waves. Furthermore, it was demonstrated that with increasing energy, the bump in flux at 90° PA, characteristic of the cap PADs, decreased in magnitude as the cyclotron resonance branch extended to higher pitch angles at higher energies. Lyons and Williams (1975a) analyzed the quiet-time structure of electron PADs at energies below 560 keV and observed a generally good agreement in PAD shapes with the theoretical predictions by Lyons et al. (1972). Furthermore, Lyons and Williams (1975b) reported that the storm-time electron PADs were very different from those during quiet times. In particular, the quiet-time cap distributions on the nightside were found to transform into the pancake PADs and then reform to their pre-storm structure several days after the storm. A comprehensive study by Gannon et al. (2007) analyzed electron PADs at energies of hundreds of keV based on data from Medium Electrons A instrument aboard the Combined release and Radiation Effects Satellite (CRRES). They reported that butterfly pitch angle distributions were the most prevalent type on the nightside at high L-shells, whereas on the dayside the pancake PADs constituted the dominant PAD shape.

In recent years, several statistical studies analyzed the storm-time evolution of electron PADs using data from the Van Allen Probes constellation. Ni et al. (2015) used 15 months of the Relativistic Electron Proton Telescope (REPT) data to investigate the variability of PADs of electrons with energies > 2 MeV. By fitting the PADs with a $\sin^n\alpha$ function, the authors tracked the spatiotemporal variability of the sine power n and

found that pancake PADs became more peaked at 90° PA during the storm times compared to the quiet times. The occurrence rate of the butterfly distributions were investigated in Ni et al. (2016), and it was found that at nightside MLTs at high L-shells, up to 80% of PADs can be of butterfly type, which was in good agreement with previous studies by West et al. (1973) and Gannon et al. (2007). Pandya et al. (2020) analyzed the storm-time morphology of PADs of 1.8–6.3 MeV electrons for 27 Coronal Mass Ejection (CME) and 28 Corrotating Interaction Region (CIR) driven storms using the REPT data. The authors reported a strong dependence of PAD shapes on MLT, while the dependence on the storm driver was found to be negligible. Greeley et al. (2021) used REPT data to analyze PAD evolution during enhancements of the ultra relativistic electron fluxes separately for CIR- and CME-driven storms. The study showed that CME-driven storms generally resulted in more anisotropic PADs than CIR-driven storms. Furthermore, it was shown that PADs return to their pre-storm configurations more rapidly during storms driven by CMEs.

The previous studies that used Van Allen Probes data for analyzing the pitch angle distributions have mainly concentrated on relativistic and ultra relativistic energies sampled by the REPT instrument. Observations by the Magnetic Electron Ion Spectrometer (MagEIS) have been used in several recent studies (e.g., Shi et al., 2016; Allison et al., 2018; Zhao et al., 2018) which aimed at creating statistical PAD models but did not investigate PAD evolution for different phases of geomagnetic storms. In this study, we perform, for the first time, a comprehensive statistical analysis of electron PADs sampled by the MagEIS detector at energies 30 keV–1.6 MeV. Furthermore, our study is the first one to use the Van Allen Probe dataset during the mission's entire lifespan in 2012–2019 for PAD analysis. We identify 129 storms in 2012–2019, and examine the morphology of the normalized PAD shapes for day and night MLTs at different energies.

Storm-time evolution of omnidirectional electron fluxes has been analyzed in detail in Turner et al. (2019) for both MagEIS and REPT energies. In this study, we concentrate on the PAD shapes normalized from 0 to 1. It should be noted that in the inner belt, pitch angle distributions appear relatively independent of activity (e.g., Ni et al., 2016) and exhibit very steep shapes due to larger loss cones which require higher harmonics for modeling (Zhao et al., 2018), therefore, in the present study we analyze PADs for L-values from 3 to 6. The paper consists of 5 parts. **Section 2** describes the data set and the methodology employed in this study. In **Section 3**, we analyze the storm-time PAD evolution by means of the superposed epoch analysis of 129 storms during the Van Allen Probes era. The results are discussed in **Section 4**, and the conclusions are drawn in the final section.

2 DATASET AND METHODOLOGY

2.1 Data

The Van Allen Probes mission, originally known as the Radiation Belt Storm Probes (RBSP), operated in 2012–2019 and consisted of two spacecraft, denoted as RBSP-A and RBSP-B, flying in a near-equatorial orbit with an inclination of 10.2° (Mauk et al., 2012). The apogee of the probes was at ~5.8 R_E and perigee at an altitude of ~620 km. The orbital period was equal to 9 h. The full MLT revolution was achieved every ~22 months. The L-shells sampled by Van Allen Probes range from 1.2 to around 6.2 on the nightside and 5.8 on the dayside.

The Magnetic Electron Ion Spectrometer (MagEIS) instruments aboard each of the probes measured electron flux over a broad energy range using one low-energy unit (LOW) for energies 20–240 keV, two medium-energy units (M75 and M35) for observing electron flux at energies 80 keV–1.2 MeV, and a high-energy unit (HIGH) to sample data at energies from 0.8 to 4.8 MeV (Blake et al., 2013). LOW, HIGH and M75 units were mounted at 75° to the spin axis, and the M35 unit was installed at 35° to the spin axis. Such a configuration was selected to provide broader pitch angle coverage for the MagEIS detector. In this study we employ the full data set of the MagEIS pitch angle resolved electron flux (level 3) in 2012–2019 averaged by 5 min with an assumed symmetry with respect to 90° PA. Following Zhao et al. (2018), we remove PADs for which the maximum electron flux value is below 100 $cm^{-2}s^{-1}sr^{-1}keV^{-1}$ as those PADs correspond to background levels of the MagEIS detector and are less indicative of the physics.

In order to analyze pitch angle distributions at the geomagnetic equator, it is necessary to propagate the locally measured electron flux values for each pitch angle to the equatorial plane using an appropriate geomagnetic field model. Since in this study we are concerned with variation of pitch angle shapes with increasing geomagnetic activity, the values are propagated to the magnetic equator using the TS04D storm-time model (Tsyganenko and Sitnov, 2005) with the internal field specified by the International Geomagnetic Reference Field (IGRF) model. The TS04D model requires as inputs the By and Bz components of the interplanetary magnetic field (IMF), solar wind velocity, density and dynamic pressure and the Dst index, as well as special *W* and *G* indices defined in (Tsyganenko and Sitnov, 2005). The values of the solar wind parameters superposed for 129 storms used in this study are shown in the Supporting information (**Supplementary Figure S2**).

2.2 PAD Approximation Using Fourier Sine Series

In this study we approximate equatorial electron PADs using the Fourier sine series expansion of the form:

$$j(\alpha) = A_0 + A_1 \sin\alpha + A_3 \sin 3\alpha + A_5 \sin 5\alpha, \quad (1)$$

where j is electron flux as a function of pitch angle α. It should be noted that the even terms ($\sin 2\alpha$ and $\sin 4\alpha$) represent shapes that are asymmetric around 90°, which is inconsistent with the trapped particle populations considered here, and therefore are omitted. In this study, we use the Fourier expansion up to degree 5, as this combination can effectively fit all the PAD types observed in the outer belt (shown in **Figures 1**, **2** and discussed below). We fit the values of electron flux to equatorial pitch angles in linear scale using least-squares and obtain values of the coefficients A_0, A_1, A_3 and A_5. As can be seen from **Equation 1**, the A_0 coefficient shows the value of electron flux in the edge of the loss cone and represents the minimum flux

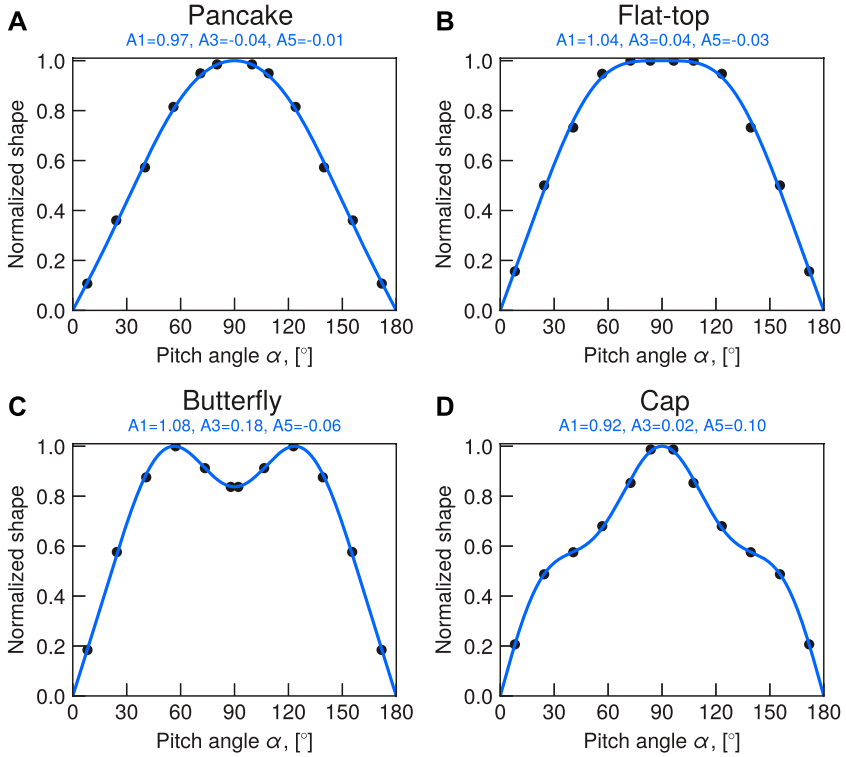

FIGURE 1 | Examples of the fitted pancake **(A)**, flat-top **(B)**, butterfly **(C)** and cap **(D)** equatorial PADs, normalized using equation 2. The dots show normalized MagEIS observations and the solid lines give fitted shapes.

value for a given PAD. Furthermore, we determine maximum value of electron flux, denoted as $j_{\max}$, within each pitch angle distribution. Carbary et al. (2011) proposed a criterion to remove low quality PAD fits, which has been used in several other studies (e.g., Ni et al., 2016). This criterion uses the normalized standard deviation of the difference between the observed and fitted electron flux and is defined as $\sigma_N = \sigma/(j_{\max} - A_0)$. The fits with the corresponding σ_N values ≤ 0.2 represent good quality fits (for details, see Carbary et al., 2011), while entries with $\sigma_N > 0.2$ were deemed as bad fits and excluded from the analysis. Examples of high- and low-quality PAD fits with the corresponding σ_N values are shown in the **Supplementary Figure S1**.

In order to normalize PADs to span from 0 to 1, we apply the following equation to the coefficients A_i, $i = \{1, 3, 5\}$:

$$\tilde{A}_i = \frac{A_i}{j_{\max} - A_0}, \tag{2}$$

where $\tilde{A}_i$ denotes the normalized value of the respective coefficient A_i. It should be noted that the PAD shapes normalized by **Equation 2** do not carry information about the flux levels and only reflect the shape of the distributions. In this study we analyze the storm-time evolution of these normalized pitch angle shapes for day and night MLTs at energies 30 keV–~1.6 MeV. The dependencies observed here are used to create a PAD model in the outer radiation belt, which is presented in Smirnov et al. (2022).

Figure 1 shows examples of the four main types of pitch angle distributions observed in the outer radiation belt region, namely the pancake, flat-top, butterfly and cap PADs, fitted using **Equation 1** and normalized by **Equation 2**. Note that while distinguishing these shapes is useful for discussions, we do not assign these discrete categories to our PADs but keep describing them through the continuous A values. Generally, the pancake PAD shape, shown in **Figure 1A**, resembles the first sine harmonic, and therefore has a large value of the corresponding coefficient A1 and low values of coefficients before the third and fifth terms (A3 and A5, respectively). The A3 coefficient corresponding to the sin (3α) term shows contribution of the butterfly shape. Since sin (3α) exhibits two peaks at 30° and 150° PA with a minimum at 90°, it can be used together with the first sine harmonic to approximate butterfly PADs (an example is given in **Figure 1C**). The flat-top PAD shape (**Figure 1B**) corresponds to high values of A1 with low values of A3, and small negative values of A5. The cap distributions (**Figure 1D**) can be fitted by a combination of the first and fifth sine harmonics. The sin (5α) function has 3 peaks (at 30°, 90° and 150°) with two depletions in between of the

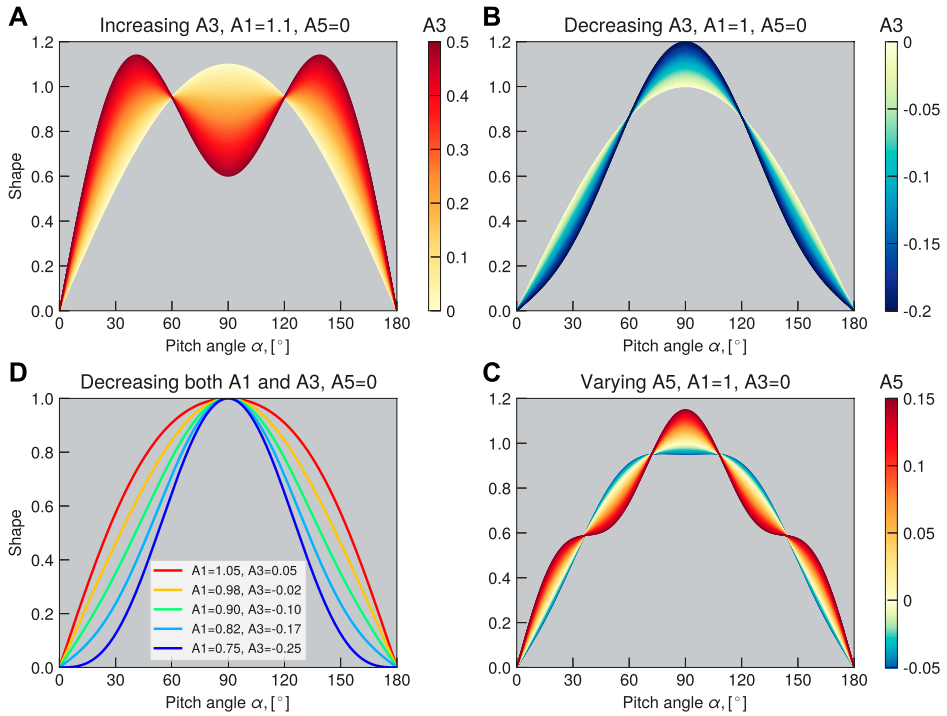

FIGURE 2 | Sketches of PAD shapes resulting from different combination of the A1, A3 and A5 coefficients. **(A)** Increasing the butterfly coefficient A3 under fixed A1 and A5 = 0 leads to stronger 90° minima; **(B)** negative values of A3 (also under fixed A1 and A5 = 0) lead to more anisotropic pancake distributions; **(C)** decreasing both A1 and A3 also creates steeper pancake PADs; **(D)** Negative A5 values result in flat-top PADs, while positive A5 values correspond to cap PAD shapes.

peaks. In combination with the general pancake shape given by $\sin(\alpha)$ it can well fit the head-and-shoulder structure.

In **Figure 2** we show different combinations of the pancake (A1), butterfly (A3) and cap (A5) coefficients, and the resulting PAD shapes. In panel (a), we fix A1 = 1.1 and A5 = 0 and start increasing the A3 magnitude from 0 to 0.5. It can be seen that for A3 = 0 a pancake shape is observed, while under higher A3 values butterfly PADs are created, and the 90° minimum becomes more pronounced. In **Figure 2B**, the A3 coefficient is decreased from 0 to -0.2. As a result, the pancake distribution becomes steeper (i.e., the anisotropy increases). In panel (c) we decrease both A1 and A3 coefficients, which also results in narrower PAD shapes. Such an increase in anisotropy of electron PADs is observed on the dayside during geomagnetic storms, and will be discussed later in **Sections 3** and **4**. In **Figure 2D** we vary the cap coefficient A5 under fixed A1 and A3. When A5 is zero, a perfect pancake distribution is observed. When A5 becomes negative, there is a transition of pancake PADs into the flat-top distributions. When A5 increases and becomes positive, cap distributions are produced. It should be noted that in case of the butterfly distributions, the A3 coefficient can increase to relatively large values (up to 0.7), while only small A5 values (0.05–0.15) are needed to resolve the head-and-shoulders PAD shape. As can be seen from **Figures 1**, **2**, the Fourier approximation fits well all main types (pancake, butterfly and cap) of equatorial pitch angle distributions. Other PAD shapes can also be resolved by this approximation, for instance, the field-aligned distributions (e.g., Clark et al., 2014, see also **Supplementary Figure S5**).

3 SUPERPOSED EPOCH ANALYSIS OF STORM-TIME PAD EVOLUTION

3.1 L and MLT Dependence

In this section, we analyze evolution of the PAD shapes in the outer radiation belt for day and night MLTs during geomagnetic storms in 2012–2019. To select the storm events for this analysis, we follow the methodology of Turner et al. (2019). As a proxy of the magnetic storm strength, we use the SYM-H index. We select events corresponding to the minimum SYM-H of less than -50 nT, while also requiring that there are no storms 2 days before nor after the event in question, to avoid the repeat events. Using this procedure, we find 129 storms throughout the Van Allen Probes era (the list of storms from October 2012 until October 2017 is given in Turner et al. (2019), their table A1, and the additional events in starting from October 2017 and until the end of the Van Allen Probes mission in late 2019 are listed in **Table 1**). **Figure 3A** shows the SYM-H index, solar wind (SW) dynamic pressure (Pdyn) and SW electric field (-v·Bz) superposed for the storms used in this study. Following Turner et al. (2019), we select the

TABLE 1 | Additional list of geomagnetic storms in October 2017—September 2019 used in this study (storms before October 2017 are listed in Turner et al. (2019) (their Table A1).

Number	Date (yyyy/mm/dd)	Time UT of min (SYM-H)
1	2017/10/14	05:35
2	2017/11/08	04:05
3	2017/11/21	06:50
4	2018/02/27	13:00
5	2018/03/10	04:35
6	2018/03/18	21:45
7	2018/04/20	09:30
8	2018/05/06	02:30
9	2018/06/01	07:15
10	2018/08/26	07:10
11	2018/09/11	10:10
12	2018/09/22	07:45
13	2018/10/07	21:50
14	2018/11/05	06:00
15	2019/05/11	03:10
16	2019/05/14	07:50
17	2019/08/05	11:45
18	2019/09/01	06:25
19	2019/09/05	05:20

values of indices, as well as PAD shape coefficients, starting from 84 h before the SYM-H minimum for each storm and up to 84 h after the minimum. The data are binned into 3-h epochs with the zero epoch corresponding to the time of SYM-H minimum. For the spatial binning, 0.2 L was selected as an appropriate step.

In **Figure 3**, the rows (b-e) show the superposed evolution of the PAD shape coefficients A1, A3 and A5 for 58 keV, as well as a higher energy of 735 keV for day (09–15 h) and night (21–03 h) MLTs. In each subplot, the *x*-axis represents the time epochs with respect to min (SYM-H), and the *y*-axis gives the McIlwain L parameter (Lm), calculated using the TS04D storm-time model. The color-coded values of the pancake (A1), butterfly (A3) and cap (A5) coefficients in these coordinates are shown in the left, middle and right columns, respectively. The corresponding standard deviations and number of points in each bin are shown in the Supporting information (**Supplementary Figure S3**). In **Figure 3** we concentrate on two energies, while the energy dependence will be later generalized in **Section 3.2**.

At lower energies on the dayside, shown in **Figure 3B**, the pancake coefficients A1 generally decrease from 0.9 to 0.7 with decreasing L-values. The same can be seen for the A3 coefficients that turn from around zero at L = 6 to negative values of approximately -0.2 at L = 3. When both A1 and A3 coefficients decrease, the pancake distributions become narrower (see **Figure 2C**). At the same time, the cap coefficient shows positive values at L = 3.5- ~ 5.6 and has a maximum at L ~ 4. This indicates that at a broad range of L-values, the cap distributions will be present (see also **Figure 5**), and that they are most pronounced around $L \sim 4$. In **Figure 3**, the row (c) shows the storm-time evolution of the coefficients for night MLTs at the same energy of 58 keV.

Figure 3D shows the evolution of the PAD coefficients for the 735 keV MagEIS energy channel. For this energy, a very strong evolution during the geomagnetic storms can be observed. Based on the row (d), two regions separated by L ~5.2 can be qualitatively defined during pre-storm times. At L < 5.2 the A1 values are around 1.1 which indicates broad pancake shapes. At L > ~5–5.2, the A3 coefficient becomes close to zero and turns negative at higher L values. At the same time, the pancake coefficient A1 decreases, which corresponds to steeper pancake PADs (the cap coefficient at high L-shells remains close to zero). When approaching the storm's main phase, both A1 and A3 decrease which can be observed down to L ~4.5. This indicates that during the main phase of the storm, the pancake distributions at higher L-shells become steeper, which is also demonstrated in **Figure 4D**. The coefficients return to their pre-storm configuration in the slow recovery phase.

In contrast, on the nightside, the butterfly coefficients A3 increase at high L-shells when approaching the storm's main phase. In **Figure 3E**, one can also distinguish two distinct regions separated by L = 5. At L < 5, the A3 coefficient is small with values around zero, while at L higher than 5, the A3 values are much larger, both for quiet and disturbed times. The A3 values during the pre-storm phase reveal the contribution of quiet-time drift shell splitting, whereas those around the maximum of the dynamic pressure indicate a combination of the drift shell splitting and magnetopause shadowing. It can be seen that at L > 5, the values of the pancake coefficient decrease, whereas the butterfly coefficient exhibits a significant increase around the main phase (see also **Supplementary Figure S4**). This means that the resulting PADs will have a stronger minimum around 90° PA. After the drop in dynamic pressure, the A3 values return to their original value range. It is worth mentioning that this recovery is faster than on the dayside. Indeed, already at 12–18 h after the min (SYM-H) the A3 and A1 coefficients are restored to their quiet time range for nightside MLTs, whereas on the dayside it takes 36–48 h to return to the pre-storm configuration. In **Figure 5** one can see that for higher energies, the butterfly coefficient becomes even more pronounced. Interestingly, at L between 3.5 and 5, one observes the steepening of the pancake distributions at nightside MLT during the storm-times, which will be discussed in detail below. It is also worth noting that the standard deviations of the *A* coefficients increase around the main phase of the storm (**Supplementary Figure S3**). This indicates that although our analysis well depicts the average storm-time behavior of electron PADs, geomagnetic storms correspond to a variety of complex processes (e.g., Reeves et al., 2003) that may not be captured without distinguishing other factors, such as the storm driver, the storm strength, etc.

Figure 4 shows the normalized PAD shapes for the four phases of the geomagnetic storms. In the top row, we show the SYM-H index, solar wind dynamic pressure and y-component of the solar wind electric field superposed for 129 storms analyzed in this study. To demonstrate the PAD shapes corresponding to different phases of the storms, we select 4 epochs, the first one at around 54 h before the SYM-H minimum (indicating the pre-storm conditions), the second one coinciding with the maximum of the SW dynamic pressure (3 h before min (SYM-H), indicative of the main phase conditions), the third one at 12 h past the SYM-H

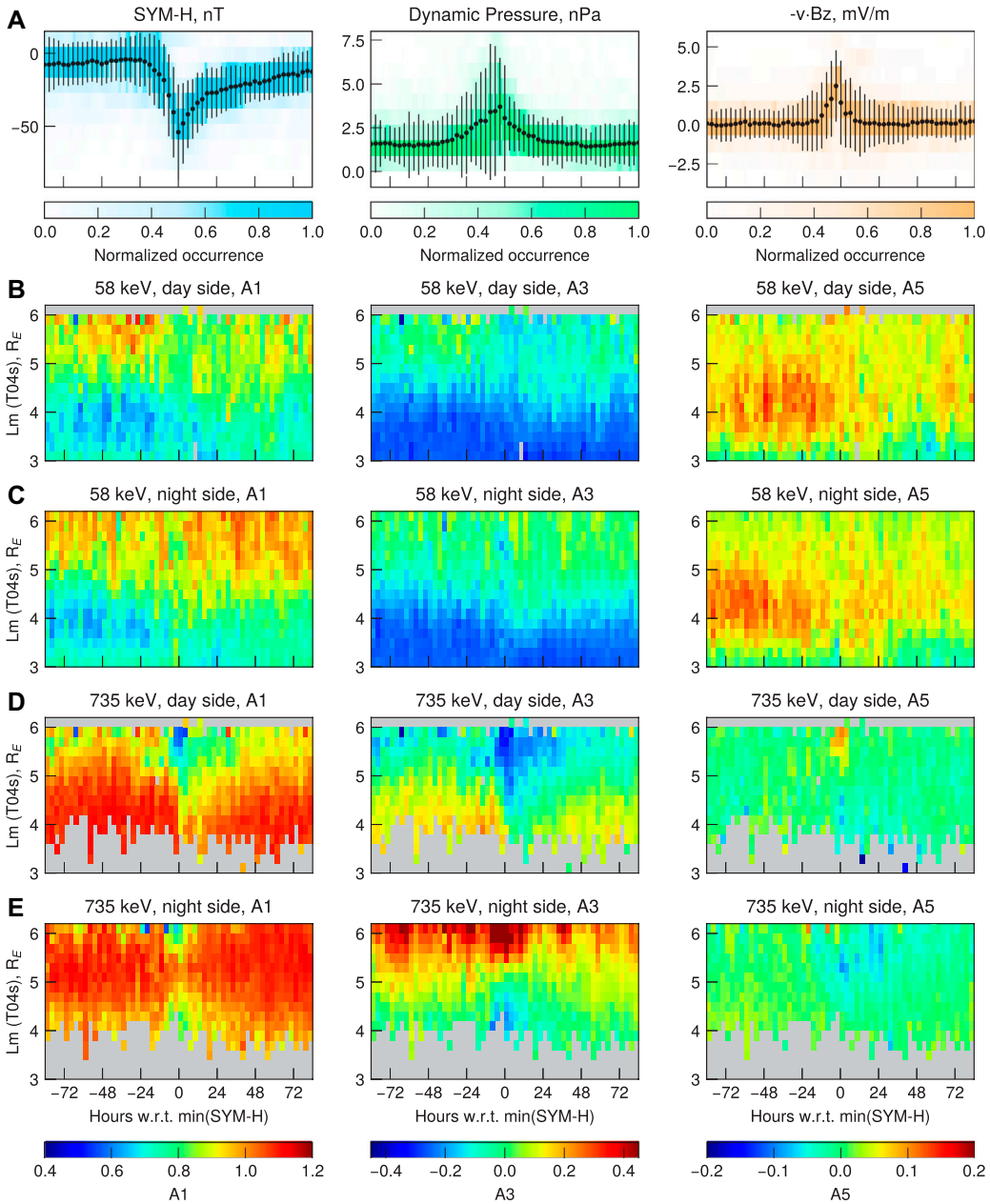

FIGURE 3 | (A) SYM-H index, SW dynamic pressure and electric field superposed for 129 storms in 2012–2019, **(B)** 3-h averaged dayside values of the A1 (pancake), A3 (butterfly) and A5 (cap) coefficients for 58 keV electrons, binned by the epochs (with respect to the SYM-H index minimum) and Lm. The coefficients in the same format for nightside evolution of 58 keV coefficients is shown in row **(C)**. The storm-time evolution of the 735 keV electron PADs for day- and nightside is given in rows **(D)** and **(E)**, respectively.

minimum (referred to as "fast recovery"), and the fourth epoch at 69 h after min (SYM-H) (i.e., in the "slow recovery"). These four epochs are marked on the superposed SYM-H, Pdyn and SW electric field plots. In **Figure 4**, the row (B) shows normalized PAD shapes for the 58 keV MagEIS channel on the dayside. The pitch angle distributions at low L-values (L < 3.5) exhibit pancake shapes, while at L ~ 3.5, the PADs transition into cap shapes (the morphology of cap PADs with respect to energy, L and MLT is described in detail in the following subsection). In the row (C) the PAD shapes are evaluated for 58 keV electrons at nightside MLTs. Generally, they look similar to the dayside shapes, except during the main phase (slice 2) where the nightside PADs exhibit pancake shapes for $L > 5.2$ while on the dayside distinct cap distributions can be observed. These results are in line with previous observations reported by Lyons and Williams (1975a). They showed that at energies of tens to hundreds of

keV there is a loss of head-and-shoulder structure during the main phase of the storm. The cap distributions generally arise due to interactions with the plasmaspheric hiss waves (e.g., Lyons et al., 1972). Due to erosion of the plasmasphere around the main phase, cap distributions transition into the pancake PADs. During the recovery phase, the plasmapause extends to higher L-values, and interactions with plasmaspheric hiss cause the quiet-time cap distributions to re-form.

In **Figure 4** (row D), we show the PAD shapes of the 735 keV electrons on the dayside (09 < MLT < 15). It can be seen that for L > 3.5, the distributions during pre-storm conditions exhibit pancake shapes. During the main phase, as noted above and shown in **Figure 4D**, the pancake distributions become narrower and then gradually recover to their original broader shapes. The magnetosphere is compressed around the main phase of the storm, which is reflected in the peak of the SW dynamic pressure (**Figure 4A**). This compression is more pronounced at dayside MLTs and gives rise to a westward electric current which will move ions and electrons inwards and adiabatically increase their kinetic energy (Walt, 2005). In this case, the third adiabatic invariant breaks down, whereas the first two invariants are conserved. Equatorially mirroring particles experience the highest adiabatic energy change. When comparing 90° particles with other pitch angles after inward transport, the 90° particles originated from the lowest energies where the phase space density was highest, explaining why the PAD is more peaked at 90° than

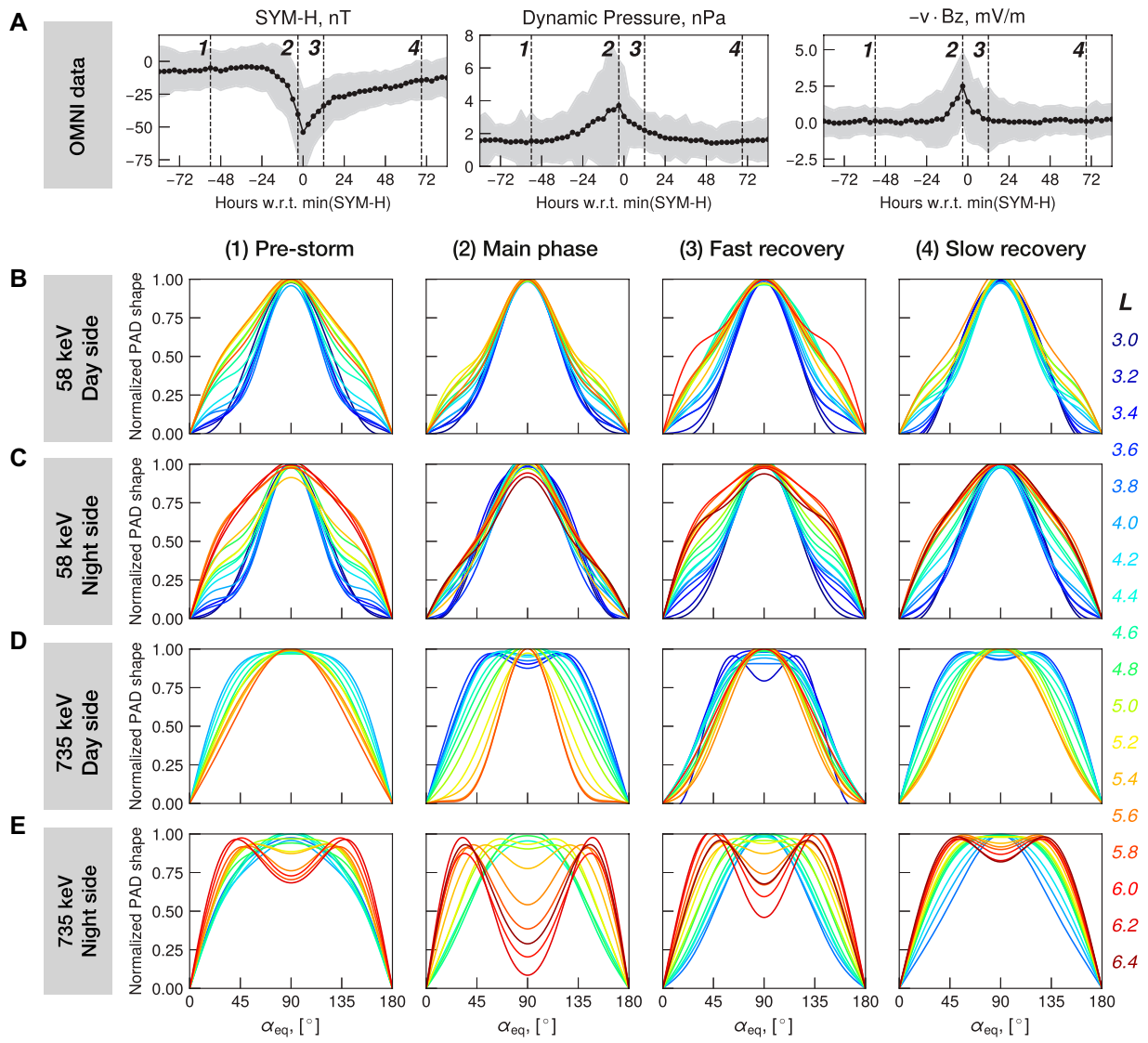

FIGURE 4 | (A) Superposed SYM-H index, SW dynamic pressure and electric field. The dashed lines denote epochs at which the PAD shapes are shown below. **(B)** Normalized PAD shapes of 58 keV electrons for 4 phases of the storm at dayside MLT. The lines are colored by the Lm values shown in a legend below. **(C)** Same as (b) but for the nighttime MLT. **(D)** Normalized PAD shapes for 735 keV electrons at dayside, and **(E)** at nightside.

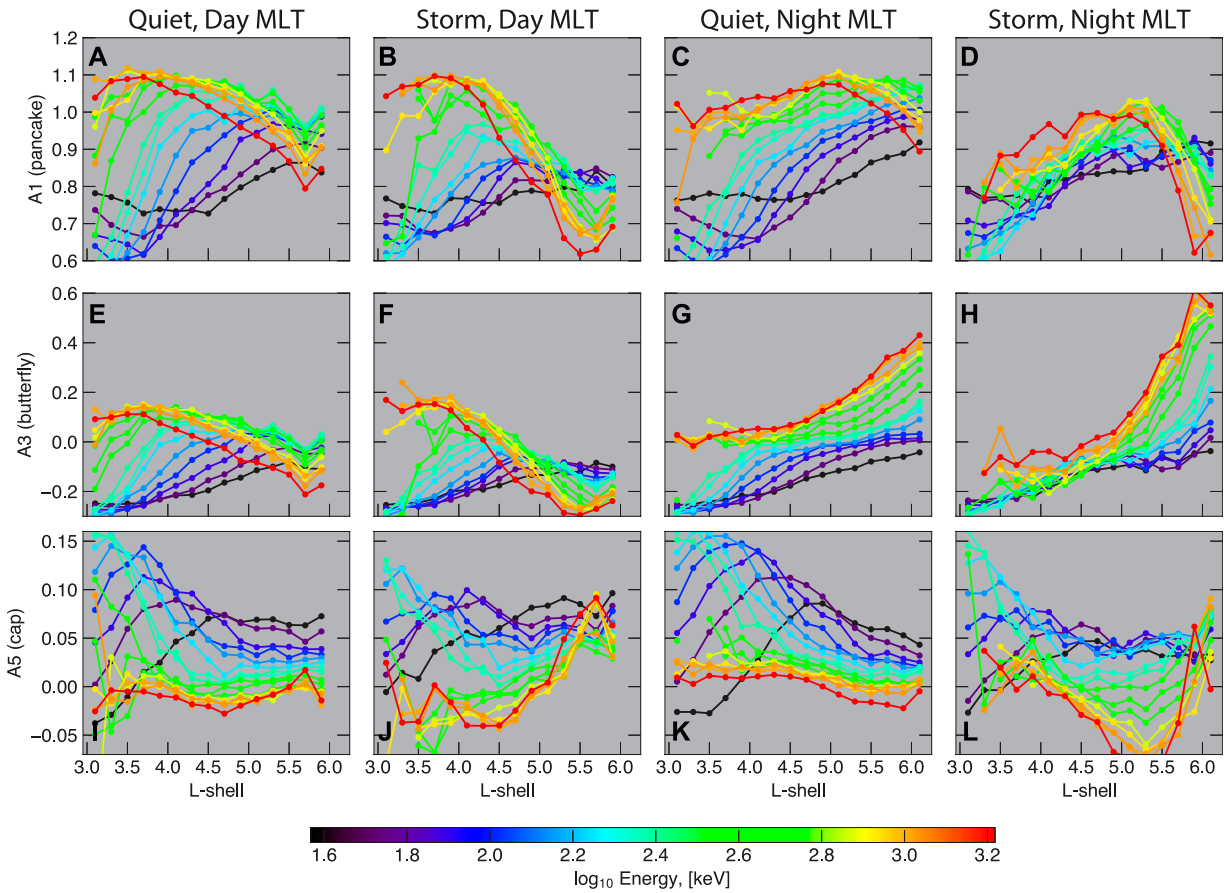

FIGURE 5 | Energy dependence of the PAD shape coefficients for pre-storm and main phase conditions at day and night MLT sectors.

before. As the system goes into the recovery, the pitch angle scattering and radial diffusion smooth out these highly anisotropic pancake distributions into their broader pre-storm shapes (Walt, 2005), which can be seen in slices 3 and 4 in **Figure 4D**. One interesting feature following the main phase is the appearance of the butterfly distributions in the inner zone. This has been previously attributed to the magnetosonic waves (e.g., Ni et al., 2016) and hiss waves (Albert et al., 2016).

The normalized PAD shapes of the 735 keV electrons at nightside MLTs for the 4 storm phases are demonstrated in **Figure 4** (row E). Our statistics cover L from 3 to around 6.4 for nightside MLTs, and for the pre-storm conditions butterfly distributions are observed at L = 5.6–6.4. At L = 5–5.6, we observe the flat-top distribution shapes (as a transition region between butterfly and pancake PADs), and pancake distributions for L < 5. The pre-storm butterflies observed on the nightside at high L-shells are indicative of the quiet-time drift shell splitting effects. Roederer (1967) showed that due to the asymmetry of the geomagnetic field particles starting at the same point but with different pitch angles will end up at different radial distances at the opposite side of the magnetosphere. If electrons start from the same point on the nightside, the near equatorially-mirroring particles would drift further from the Earth on the dayside than particles of lower pitch angles. The PA-dependence of the drift paths leads to the formation of the butterfly distributions. While the drift-shell splitting is not energy dependent, it has been well established that a negative radial gradient in phase space density (PSD) is a necessary component to create the butterfly PADs (Roederer, 1967). At lower energies, the flux gradient is smaller than at high energies (see e.g. **Figure 3** in Turner et al., 2019), and therefore the drift shell splitting has less influence on the PADs. This is consistent with the absence of butterflies at low (58 keV) energies (**Figures 4B,C**). In **Figure 3E**, **Figure 4E** we demonstrate that during the main storm phase, the 90°-minimum in the butterfly distributions becomes stronger at high L on the nightside. In **Figure 3E** this manifests as an increase in the A3 coefficients around the maximum of the dynamic pressure. In **Figure 4E**, slice 2 shows that the butterfly PADs also extend to lower L-values. With increasing dynamic pressure, drift shell splitting intensifies and thus the butterfly distributions can be observed at lower L-shells. At around L = 4.8–5.0, PADs transition into the flat-top/broad pancake and then to steeper pancake distributions at L < 4.5. In **Figure 4E**, PADs at L < 3.6 during the pre-storm phase corresponded to background levels of

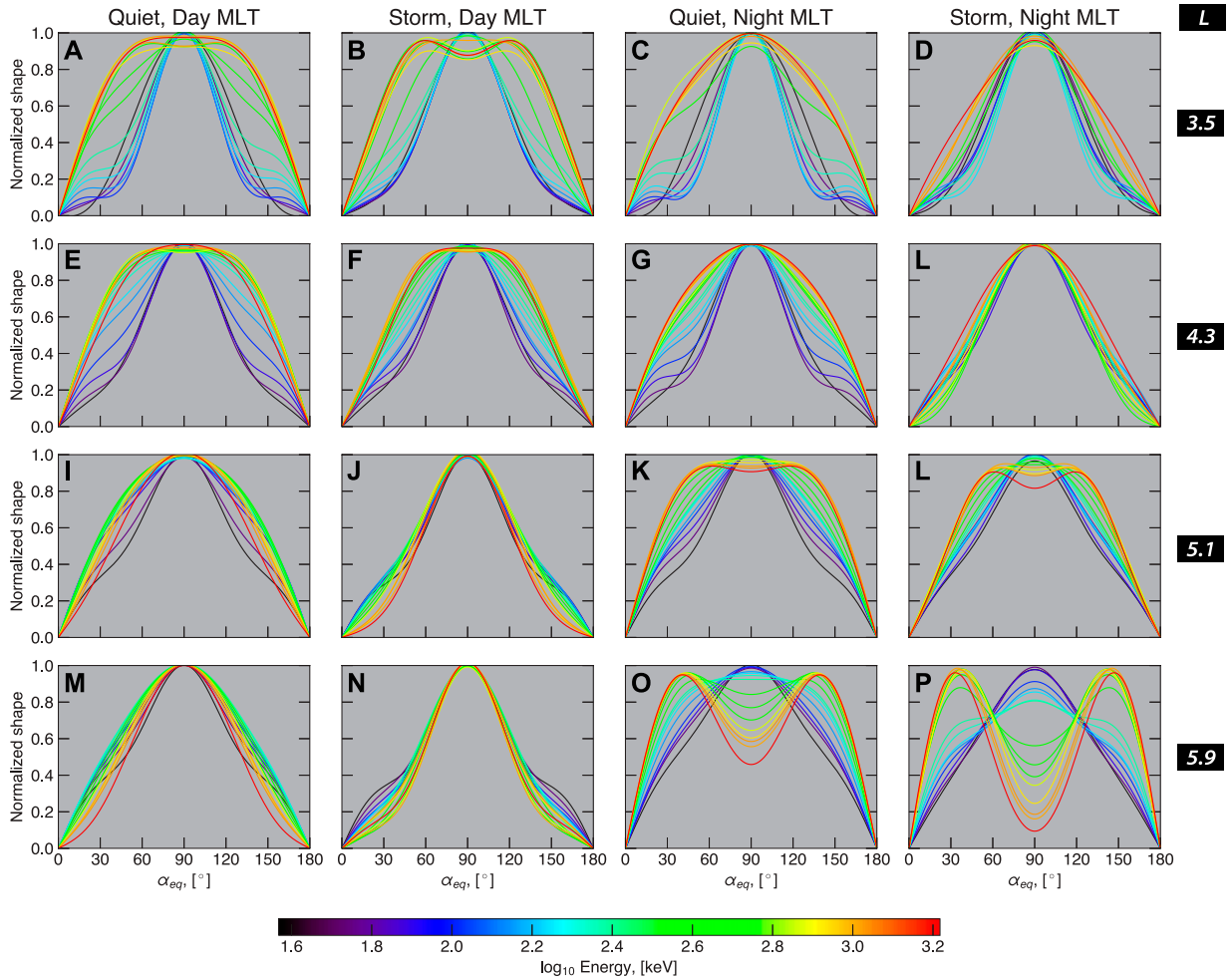

FIGURE 6 | Energy dependence of pitch angle shapes at different L-values for quiet and storm conditions on the day and nightside MLT.

electron flux and were removed, whereas after the main phase the flux values are increased in the slot region (e.g., Reeves et al., 2016), and the pitch angle distributions exhibit pancake shapes.

3.2 Energy Dependence

Figure 5 demonstrates the energy dependence of the PAD shape coefficients for L = 3—6 at day and night MLTs. The resulting PAD shapes plotted as a function of energy under several fixed values of L are shown in **Figure 6**. The values shown here are superposed for 129 storms for the pre-storm and main phase conditions. We first analyze the day-time morphology. It can be seen from **Figure 5** (A and B) that at energies of $< \sim$ 100 keV, the pancake coefficient A1 appears similar for storm and quiet conditions. The same can be observed for the butterfly coefficient A3 in panels (E and F). At higher energies at $L < 5$, both A1 and A3 coefficients generally decrease with decreasing energy during quiet times. At the same time, in **Figure 5I**, the cap coefficient is intensified at energies of hundreds of keV and below. It is worth noting that the peak of the cap coefficient across the L-shells is strongly energy-dependent, and moves inward with increasing energy (**Figure 5I**). At higher energies the cap coefficient values are generally around zero (at $L > 3.2$), which is consistent with the theoretical results by Lyons et al. (1972) and is attributed to the fact that with increasing energy, the dominant first-order cyclotron resonance extends to higher PAs (see **Figure 4** in Lyons et al. (1972)) and pitch angle scattering can then affect all equatorial pitch angles.

During the main phase at dayside MLTs, the A1 and A3 coefficients decrease (**Figure 5**, panels B and F), which is especially evident for $L > 4.5$. At energies below 300 keV, the values of the cap coefficient remain at around 0.05 which means that the cap distributions persist at lower energies during the main phase. The cap coefficient decreases at $L < 4.5$ for energies above 300 keV and turns negative, which results in the flattop distributions (**Figure 6F**). At $L > 4.5$, the A1 and A3 coefficients decrease, while the A5 coefficient increases. This increase in the A5 coefficient corresponds to strongly anisotropic pancake PADs

(see also **Figure 4D**, slice 2) during the main phase on the dayside. Furthermore, the degree of this anisotropy increases with energy (see also **Figures 6I,J**).

During the pre-storm phase the butterfly distributions dominate at L > 5.5 on the nightside (also discussed in **Section 3.1**). In **Figure 5D** one can see that at L > 5 the pancake coefficient equals approximately 0.9–1.1, while during the main phase the values drop down to 0.6–0.8 across the MagEIS energy range. At the same time, there is a dramatic increase in the butterfly coefficient A3 at large L-shell on the nightside. For instance, at energies of ~ 300 keV the pre-storm A3 values were around 0.2, while during the main phase they are magnified by a factor of 2. Furthermore, from **Figure 6**(P) it is obvious that the 90° minimum gets stronger with increasing energy. At L of ~5, the A5 coefficient becomes negative, and as shown in **Figure 2** this corresponds to the flat-top PAD shape. At $L < 5.1$, the butterfly coefficients A3 significantly decrease at all energies (**Figure 5H**) and remains small at lower L-shells, where PADs have pancake shapes.

4 DISCUSSION

In this study we employed a Fourier sine series expansion to approximate electron pitch angle distributions. It was shown that a combination of the first, third and fifth sine harmonics can effectively fit all main types of PADs in the outer radiation belt. This approximation has previously been used for analyzing distributions of electrons in planetary magnetospheres, for instance, by Clark et al. (2014). In case of the terrestrial radiation belts, most studies fitted electron PADs to the $\sin^n(\alpha)$ function, where n shows the steepness of the distribution (larger values of n correspond to more anisotropic distributions). This approximation is very easy to use, and the resulting values can be incorporated into the radiation belts simulations (e.g., Shi et al., 2016). However, the $\sin^n(\alpha)$ function can only approximate flat-top, pancake and isotropic distributions but is not capable of fitting butterfly and cap shapes. Butterfly distributions can account for up to 80% of PADs on the nightside, and cap distributions dominate lower energies both for day and night-side MLTs during geomagnetically quiet times. Allison et al. (2018) combined two $\sin^n(\alpha)$ terms with different n values which helped two resolve the cap but not butterfly distributions. Due to the fact that different types of PADs can be linked to specific processes acting within the radiation belts, it is crucial to use an approximation that can fit all of the PAD types. We have shown (**Figures 1**, **2**) that the Fourier series are capable of resolving all main PAD shapes. Furthermore, the expression used here (**Eq. 1**) is easy to integrate over the solid angle and can be used to compute omnidirectional flux values using an analytic expression. We note that the methodology developed in this study can be extended to a range of magnetospheric problems, for instance, to analyzing pitch angle distributions of low-energy electrons and ions.

It is well-known that electrons in the inner radiation belt are stable both in terms of their amplitudes (e.g., Shprits et al., 2013), and pitch angle distributions (e.g., Zhao et al., 2018). Furthermore, electrons at energies over 1 MeV are generally absent in the inner zone (Fennell et al., 2015). Therefore, for analyzing the PAD dynamics during geomagnetic storms we concentrated on the outer radiation belt region. While several studies have already used RBSP data for analyzing the storm-time PAD evolution (e.g., Ni et al., 2015; Ni et al., 2016; Drozdov et al., 2019; Ni et al., 2020; Pandya et al., 2020; Greeley et al., 2021), they focused on relativistic and ultra-relativistic energies sampled by the REPT detector. In the current paper we concentrated on lower energies, from 30 keV to around 1.6 MeV, using observations by the MagEIS detector during the entire lifespan of the Van Allen Probes mission in 2012–2019. Our study has a certain overlap in energies (> 1 MeV) with the previous works by Pandya et al. (2020) and Greeley et al. (2021) and therefore our results can also be compared to those studies. Due to the fact that RBSP orbit was revolving in MLT quite slowly, with a full revolution being completed every 22 months, the statistics for analyzing both MLT and storm driver dependence would be limited, and therefore in the present study we concentrated on the day- and night-time PAD morphology. Furthermore, Pandya et al. (2020) showed that at least for relativistic energies, the dependence of PAD evolution on storm driver was negligible.

It has been shown that the morphology of electron PADs is significantly different during geomagnetically quiet times compared to the active times (Lyons and Williams, 1975b). During periods of low geomagnetic activity, pitch angle distributions at energies below ~300 keV exhibit cap (or, head-and-shoulder) shapes. This configuration results from cyclotron and Landau resonance with hiss waves, and is strongly energy-dependent (Lyons et al., 1972; Lyons and Williams, 1975a). In particular, in **Figures 4**, **5** we demonstrate that the cap coefficient A5 exhibits a peak at L ~ 5 for 37 keV electrons, and then moves inward in L with increasing energy, which is in line previous results of (e.g., Shi et al., 2016) who reported that peak of PAD anisotropy, corresponding to cap PADs, was moving to smaller L-values under increasing energy. The same conclusion was reported by Allison et al. (2018). For each energy, Allison et al. (2018) highlighted regions where the combination of two $\sin^n(\alpha)$ terms was performing better than a single sine term. Those regions corresponded to the cap distributions. It was found that the extent of this region diminished with increasing energy, but was practically independent of Kp levels. In the current study we observed loss of the head-and-shoulders structure during the main phase of the storm at nightside MLTs, which is consistent with previous studies by Lyons and Williams (1975b) and Zhao et al. (2018). Due to the fact with increasing geomagnetic activity the plasmasphere is eroded (e.g., Goldstein et al., 2019), there would be no hiss waves at higher L-shells that could generate cap PADs (see e.g., Lyons and Williams, 1975b). Furthermore, during active times the low-energy particles are injected from the tail (e.g., Reeves et al., 1996). Turner et al. (2015a) demonstrated that injections of electrons with energies below 240 keV can be frequently observed within the geostationary orbit. Furthermore, Motoba et al. (2020) performed a superposed epoch analysis of dispersionless injections using RBSP data and showed that the corresponding pitch angle distributions of tens-of-keV electrons

exhibited pancake shapes. Therefore, the transformation of cap PADs into pancakes during the main phase at low energies on the nightside (**Figures 3C**, **Figure 4C**) is likely due to the combination of the plasmasphere erosion and particle injections from the tail.

At energies $>\sim 150$ keV, pancake distributions are observed on the dayside at $L > 4$ (**Figure 6**). The pancake distributions generally result from the particle pitch angle diffusion (e.g., West et al., 1973). During geomagnetically quiet times, pancake distributions exhibit relatively broad shapes. During active times, we observe narrowing of the pancake PADs. During the main phase, PADs at high L-shells ($L > 5.8$) become strongly anisotropic, but distributions at lower L-shells still have broad shapes. The opposite is observed during the fast recovery phase (approximately 12 h after the SYM-H minimum) - the narrowing moved inwards in L-shell, while at higher L-values the distributions already started to recover to their pre-storm shapes. In the slow recovery phase, the distributions returned to their pre-storm morphology. These results go well with previous findings of Pandya et al. (2020) and Greeley et al. (2021) who also reported narrowing of the pancake PADs during the main phase of the storm. These signatures (narrowing of pancake PADs which progressively moving inward and the subsequent relaxation to pre-storm shapes) are indicative of the inward radial diffusion (Schulz and Lanzerotti, 1974).

On the nightside, the PAD morphology is very different than on the dayside. At energies >200 keV the quiet-time distributions are mainly of pancake type at $L < 5$. For L-shells around 5 and energies of around 200 keV, the pancake distributions transform into flat-top PADs. Then, at higher energies there is an emerging minimum at 90° PA which intensifies with increasing energy (see **Figure 6**). Energy dependence of the butterfly distributions can be explained as follows. During quiet conditions at $L > 5$ the equatorially mirroring particles in the nightside are transported to larger radial distances in the dayside than the lower PA particles, which is known as magnetic drift shell splitting (e.g., Roederer, 1967; Sibeck et al., 1987). This effect, however, depends only on magnetic field and not on particle energy. At the same time, it has been well established that a negative radial gradient in PSD is a necessary component for the drift shell splitting to be effective (Roederer, 1967). Recently, Turner et al. (2019) presented a superposed epoch analysis of omnidirectional electron flux observed by the Van Allen Probes mission. In their **Figure 2** one can see that flux gradient in L at lower energies is relatively flat. On the other hand, at higher energies there is a strong negative flux gradient which enables the drift shell splitting to have the full effect on pitch angle distributions and create butterfly PADs. Therefore, with increasing energy the drift shell splitting effects become more evident due to stronger radial gradients in flux.

During the main phase of the storm, the butterfly distributions on the nightside are intensified (**Figures 4–6**). Such an intensification is most likely due to a combination of the enhanced drift shell splitting and magnetopause shadowing. While the magnetopause is usually located at radial distances of $>10R_E$, it is well-known that during active times the last closed drift shell can move inward down to $L \sim 4$. Equatorially mirroring electrons travel to larger distances than low-PA electrons and therefore can get lost to the magnetopause, creating the butterfly distributions. The storm-time butterfly distributions are not observed below $L = 5$ (see **Figures 3–5**). At L around 5, one can observe a transition of the butterfly into flat-top PADs. Horne et al. (2003) proposed two potential explanations for such a transition at higher energies, namely the inward radial diffusion and wave particle interactions. They concluded that the radial diffusion could be an important factor but did not account for energy dependence of flat-top PADs. By considering the cyclotron resonance with whistler mode chorus waves in presence of low plasma densities, Horne et al. (2003) were able to reproduce a realistic energy dependence of the flat-top PADs.

In this study, we analyzed the normalized electron pitch angle distributions measured by the MagEIS detector onboard the Van Allen Probes mission. The storm-time spin-averaged electron flux intensities were previously investigated by Turner et al. (2019), and it was reported that electrons of different energies exhibited a significantly different response to geomagnetic storms (see also Turner et al., 2015b). In our study, the storm-time morphology of the PAD shapes was also found to vary greatly with energy. It is worth noting that the results presented here can be combined with averaged picture of the spin-averaged electron flux evolution from Turner et al. (2019), as both the flux intensities and pitch angle distribution shapes are important for distinguishing between the loss and acceleration processes (e.g., Chen et al., 2005). Furthermore, due to complex mechanisms acting in the outer belt during the storm times, different particle populations can evolve into one another. For instance, electrons with energies up to tens of keV (the so-called seed population) can be injected during the substorm activity and produce waves that can energize the tens to hundreds of keV electrons to higher energies. In order to investigate these processes in detail, it is beneficial to analyze phase space densities under different values of μ and K, which gives an opportunity to see the time lags between the different populations (see, for instance, Boyd et al., 2016). We note, however, that in the current study we did not make any assumptions on the processes acting within the outer belt, and therefore the PAD shapes averaged for different storm epochs and energies obtained in this study already include part of the information on the mechanisms mentioned above and provide a good indication of the averaged storm-time behavior of the 30 keV–1.6 MeV electrons.

5 CONCLUSIONS

Using the full MagEIS data set of pitch angle resolved electron flux at energies 30 keV - ~1.6 MeV in 2012–2019, we analyze equatorial electron PADs at L = 3–6. We use a combination of the first, third and fifth sine harmonics to approximate the pitch angle distributions. The corresponding expression can be

analytically integrated, and the values of coefficients before the three terms relate to the main PAD shapes. We perform a superposed epoch analysis of 129 strong geomagnetic storms during the Van Allen Probes era for day and night MLTs. Our findings are as follows.

1. Cap distributions are mainly present at energies < 300 keV, and their spatial extent in L shrinks with increasing energy. During the main phase on the nightside, cap PADs transform into pancakes at $L > 4.5$, likely due erosion of the plasmasphere and particle injections from the tail. During the recovery phase, the cap distributions are re-formed at high L-shells.
2. At higher energies on the dayside, the distributions are mainly pancake. They exhibit broad shapes during quiet conditions and become more anisotropic during the main phase of the storm due to the field's compression. The degree of this anisotropy smoothly increases with energy.
3. The butterfly distributions can be observed on the nightside at $L > 5.6$ during the pre-storm phase. During the main phase, the butterfly PADs can be found at lower L-values (down to L = 5), likely due to the combination of drift shell splitting and magnetopause shadowing. Furthermore, the 90° minimum intensifies with increasing energy. This is consistent with stronger negative radial flux gradients at higher energies, which allow the drift shell splitting to create stronger butterfly PADs.
4. On the nightside, there is a transition region between the butterfly and pancake PADs, populated by the flat-top distributions. During quiet conditions, this transition is located at $L \sim 5.5$ and moves inward to $L \sim 5$ during the main phase of the storm.

The PAD shape coefficients for different L-shells, MLTs and phases of geomagnetic storms obtained in this study can be used for comparisons with the results achieved through the existing wave models when the flux magnitude is taken into consideration, as well as the outputs of the physics-based radiation belt simulations, in terms of PAD shapes. Furthermore, the dependencies reported here can further be used to improve the existing empirical models of the pitch angle distributions in Earth's outer radiation belt.

DATA AVAILABILITY STATEMENT

The original contributions presented in the study are included in the article/**Supplementary Material**, further inquiries can be directed to the corresponding author.

AUTHOR CONTRIBUTIONS

AS and YS conceived the idea of the study. AS performed the analysis with input from YS, HA, NA, AD and PK. AS wrote the manuscript; YS, HA, NA, AD, PK, GR, DW and AAS contributed to structuring and editing the manuscript.

FUNDING

This project has received funding from the European Union's Horizon 2020 research and innovation programme under grant agreement No. 870452 (PAGER). HA was supported by the Alexander von Humboldt foundation.

ACKNOWLEDGMENTS

AS acknowledges support from the International Space Science Institute (ISSI—Bern, Switzerland) through the ISSI team on "Imaging the Invisible: Unveiling the Global Structure of Earth's Dynamic Magnetosphere".

SUPPLEMENTARY MATERIAL

The Supplementary Material for this article can be found online at: https://www.frontiersin.org/articles/10.3389/fspas.2022.836811/full#supplementary-material

REFERENCES

Albert, J. M., Starks, M. J., Horne, R. B., Meredith, N. P., and Glauert, S. A. (2016). Quasi-Linear Simulations of Inner Radiation belt Electron Pitch Angle and Energy Distributions. *Geophys. Res. Lett.* 43, 2381–2388. doi:10.1002/2016gl067938

Allison, H. J., Horne, R. B., Glauert, S. A., and Del Zanna, G. (2018). Determination of the Equatorial Electron Differential Flux from Observations at Low Earth Orbit. *J. Geophys. Res. Space Phys.* 123, 9574–9596. doi:10.1029/2018ja025786

Artemyev, A. V., Agapitov, O. V., Mozer, F. S., and Spence, H. (2015). Butterfly Pitch Angle Distribution of Relativistic Electrons in the Outer Radiation Belt: Evidence of Nonadiabatic Scattering. *J. Geophys. Res. Space Phys.* 120, 4279–4297. doi:10.1002/2014ja020865

Blake, J. B., Carranza, P. A., Claudepierre, S. G., Clemmons, J. H., Crain, W. R., Dotan, Y., et al. (2013). "The Magnetic Electron Ion Spectrometer (MagEIS) Instruments Aboard the Radiation Belt Storm Probes (RBSP) Spacecraft," in *The Van Allen Probes Mission*. Editors N. Fox and J. L. Burch (Boston, MA: Springer), 383–421. doi:10.1007/978-1-4899-7433-4_12

Boyd, A. J., Spence, H. E., Huang, C. L., Reeves, G. D., Baker, D. N., Turner, D. L., et al. (2016). Statistical Properties of the Radiation Belt Seed Population. *J. Geophys. Res. Space Phys.* 121, 7636–7646. doi:10.1002/2016ja022652

Carbary, J., Mitchell, D., Paranicas, C., Roelof, E., Krimigis, S., Krupp, N., et al. (2011). Pitch Angle Distributions of Energetic Electrons at Saturn. *J. Geophys. Res. Space Phys.* 116. doi:10.1029/2010ja015987

Chen, Y., Friedel, R. H. W., Henderson, M. G., Claudepierre, S. G., Morley, S. K., and Spence, H. E. (2014). REPAD: An Empirical Model of Pitch Angle Distributions for Energetic Electrons in the Earth's Outer Radiation belt. *J. Geophys. Res. Space Phys.* 119, 1693–1708. doi:10.1002/2013ja019431

Chen, Y., Friedel, R., Reeves, G., Onsager, T., and Thomsen, M. (2005). Multisatellite Determination of the Relativistic Electron Phase Space Density at Geosynchronous Orbit: Methodology and Results during Geomagnetically Quiet Times. *J. Geophys. Res. Space Phys.* 110. doi:10.1029/2004ja010895

Clark, G., Paranicas, C., Santos-Costa, D., Livi, S., Krupp, N., Mitchell, D. G., et al. (2014). Evolution of Electron Pitch Angle Distributions across Saturn's Middle Magnetospheric Region from MIMI/LEMMS. *Planet. Space Sci.* 104, 18–28. doi:10.1016/j.pss.2014.07.004

Drozdov, A. Y., Aseev, N., Effenberger, F., Turner, D. L., Saikin, A., and Shprits, Y. Y. (2019). Storm Time Depletions of Multi-MeV Radiation Belt Electrons Observed at Different Pitch Angles. *J. Geophys. Res. Space Phys.* 124, 8943–8953. doi:10.1029/2019ja027332

Fennell, J. F., Claudepierre, S. G., Blake, J. B., O'Brien, T. P., Clemmons, J. H., Baker, D. N., et al. (2015). Van Allen Probes Show that the Inner Radiation Zone Contains No MeV Electrons: ECT/MagEIS Data. *Geophys. Res. Lett.* 42, 1283–1289. doi:10.1002/2014gl062874

Gannon, J., Li, X., and Heynderickx, D. (2007). Pitch Angle Distribution Analysis of Radiation belt Electrons Based on Combined Release and Radiation Effects Satellite Medium Electrons A Data. *J. Geophys. Res. Space Phys.* 112. doi:10.1029/2005ja011565

Ganushkina, N. Y., Dandouras, I., Shprits, Y., and Cao, J. (2011). Locations of Boundaries of Outer and Inner Radiation Belts as Observed by Cluster and Double Star. *J. Geophys. Res. Space Phys.* 116. doi:10.1029/2010ja016376

Goldstein, J., Pascuale, S., and Kurth, W. S. (2019). Epoch-Based Model for Stormtime Plasmapause Location. *J. Geophys. Res. Space Phys.* 124, 4462–4491. doi:10.1029/2018ja025996

Greeley, A. D., Kanekal, S. G., Sibeck, D. G., Schiller, Q., and Baker, D. N. (2021). Evolution of Pitch Angle Distributions of Relativistic Electrons during Geomagnetic Storms: Van Allen Probes Observations. *J. Geophys. Res. Space Phys.* 126, e2020JA028335. doi:10.1029/2020ja028335

Hao, Y. X., Zong, Q.-G., Zhou, X.-Z., Rankin, R., Chen, X. R., Liu, Y., et al. (2017). Relativistic Electron Dynamics Produced by Azimuthally Localized Poloidal Mode ULF Waves: Boomerang-Shaped Pitch Angle Evolutions. *Geophys. Res. Lett.* 44, 7618–7627. doi:10.1002/2017gl074006

Horne, R. B., Meredith, N. P., Thorne, R. M., Heynderickx, D., Iles, R. H., and Anderson, R. R. (2003). Evolution of Energetic Electron Pitch Angle Distributions during Storm Time Electron Acceleration to Megaelectronvolt Energies. *J. Geophys. Res. Space Phys.* 108, SMP–11. doi:10.1029/2001ja009165

Lyons, L. R., Thorne, R. M., and Kennel, C. F. (1972). Pitch-Angle Diffusion of Radiation belt Electrons within the Plasmasphere. *J. Geophys. Res.* 77, 3455–3474. doi:10.1029/ja077i019p03455

Lyons, L. R., and Williams, D. J. (1975b). The Quiet Time Structure of Energetic (35-560 keV) Radiation belt Electrons. *J. Geophys. Res.* 80, 943–950. doi:10.1029/JA080i007p00943

Lyons, L. R., and Williams, D. J. (1975a). The Storm and Poststorm Evolution of Energetic (35-560 keV) Radiation belt Electron Distributions. *J. Geophys. Res.* 80, 3985–3994. doi:10.1029/ja080i028p03985

Mauk, B. H., Fox, N. J., Kanekal, S. G., Kessel, R. L., Sibeck, D. G., and Ukhorskiy, A. (2012). "Science Objectives and Rationale for the Radiation Belt Storm Probes Mission," in *The Van Allen Probes Mission*. Editors N. Fox and J. L. Burch (Boston, MA: Springer), 3–27. doi:10.1007/978-1-4899-7433-4_2

Meredith, N. P., Horne, R. B., Johnstone, A. D., and Anderson, R. R. (2000). The Temporal Evolution of Electron Distributions and Associated Wave Activity Following Substorm Injections in the Inner Magnetosphere. *J. Geophys. Res.* 105, 12907–12917. doi:10.1029/2000ja900010

Motoba, T., Ohtani, S., Gkioulidou, M., Mitchell, D. G., Ukhorskiy, A., Takahashi, K., et al. (2020). Pitch Angle Dependence of Electron and Ion Flux Changes during Local Magnetic Dipolarization inside Geosynchronous Orbit. *J. Geophys. Res. Space Phys.* 125, e2019JA027543. doi:10.1029/2019ja027543

Ni, B., Yan, L., Fu, S., Gu, X., Cao, X., Xiang, Z., et al. (2020). Distinct Formation and Evolution Characteristics of Outer Radiation belt Electron Butterfly Pitch Angle Distributions Observed by Van Allen Probes. *Geophys. Res. Lett.* 47, e2019GL086487. doi:10.1029/2019gl086487

Ni, B., Zou, Z., Gu, X., Zhou, C., Thorne, R. M., Bortnik, J., et al. (2015). Variability of the Pitch Angle Distribution of Radiation belt Ultrarelativistic Electrons during and Following Intense Geomagnetic Storms: Van Allen Probes Observations. *J. Geophys. Res. Space Phys.* 120, 4863–4876. doi:10.1002/2015ja021065

Ni, B., Zou, Z., Li, X., Bortnik, J., Xie, L., and Gu, X. (2016). Occurrence Characteristics of Outer Zone Relativistic Electron Butterfly Distribution: A Survey of Van Allen Probes REPT Measurements. *Geophys. Res. Lett.* 43, 5644–5652. doi:10.1002/2016gl069350

Pandya, M., Bhaskara, V., Ebihara, Y., Kanekal, S. G., and Baker, D. N. (2020). Evolution of Pitch Angle-Distributed Megaelectron Volt Electrons during Each Phase of the Geomagnetic Storm. *J. Geophys. Res. Space Phys.* 125, e2019JA027086. doi:10.1029/2019ja027086

Reeves, G. D., Friedel, R. H. W., Larsen, B. A., Skoug, R. M., Funsten, H. O., Claudepierre, S. G., et al. (2016). Energy-dependent Dynamics of keV to MeV Electrons in the Inner Zone, Outer Zone, and Slot Regions. *J. Geophys. Res. Space Phys.* 121, 397–412. doi:10.1002/2015ja021569

Reeves, G., Henderson, M., McLachlan, P., Belian, R., Friedel, R., and Korth, A. (1996). Radial Propagation of Substorm Injections. *Int. Conf. substorms* 389, 579.

Reeves, G., McAdams, K., Friedel, R., and O'Brien, T. (2003). Acceleration and Loss of Relativistic Electrons during Geomagnetic Storms. *Geophys. Res. Lett.* 30. doi:10.1029/2002gl016513

Roederer, J. G. (1967). On the Adiabatic Motion of Energetic Particles in a Model Magnetosphere. *J. Geophys. Res.* 72, 981–992. doi:10.1029/jz072i003p00981

Schulz, M., and Lanzerotti, L. J. (1974). *Particle Diffusion in the Radiation Belts*. New York: Springer-Verlag. doi:10.1007/978-3-642-65675-0

Selesnick, R., and Blake, J. (2002). Relativistic Electron Drift Shell Splitting. *J. Geophys. Res. Space Phys.* 107, SMP–27. doi:10.1029/2001ja009179

Shi, R., Summers, D., Ni, B., Fennell, J. F., Blake, J. B., Spence, H. E., et al. (2016). Survey of Radiation Belt Energetic Electron Pitch Angle Distributions Based on the Van Allen Probes MagEIS Measurements. *J. Geophys. Res. Space Phys.* 121, 1078–1090. doi:10.1002/2015ja021724

Shprits, Y. Y., Subbotin, D., Drozdov, A., Usanova, M. E., Kellerman, A., Orlova, K., et al. (2013). Unusual Stable Trapping of the Ultrarelativistic Electrons in the Van Allen Radiation Belts. *Nat. Phys* 9, 699–703. doi:10.1038/nphys2760

Sibeck, D. G., McEntire, R. W., Lui, A. T. Y., Lopez, R. E., and Krimigis, S. M. (1987). Magnetic Field Drift Shell Splitting: Cause of Unusual Dayside Particle Pitch Angle Distributions during Storms and Substorms. *J. Geophys. Res.* 92, 13485–13497. doi:10.1029/ja092ia12p13485

Smirnov, A., Shprits, Y., Allison, H., Aseev, N., Drozdov, A., Kollmann, P., et al. (2022). An Empirical Model of the Equatorial Electron Pitch Angle Distributions in Earth's Outer Radiation belt. *Space Weather under Rev*.

Su, Z., Zheng, H., and Wang, S. (2009). Evolution of Electron Pitch Angle Distribution Due to Interactions with Whistler Mode Chorus Following Substorm Injections. *J. Geophys. Res. Space Phys.* 114. doi:10.1029/2009ja014269

Tsyganenko, N., and Sitnov, M. (2005). Modeling the Dynamics of the Inner Magnetosphere during strong Geomagnetic Storms. *J. Geophys. Res. Space Phys.* 110. doi:10.1029/2004ja010798

Turner, D. L., Claudepierre, S. G., Fennell, J. F., O'Brien, T. P., Blake, J. B., Lemon, C., et al. (2015a). Energetic Electron Injections Deep into the Inner Magnetosphere Associated with Substorm Activity. *Geophys. Res. Lett.* 42, 2079–2087. doi:10.1002/2015gl063225

Turner, D. L., Kilpua, E., Hietala, H., Claudepierre, S., O'Brien, T., Fennell, J., et al. (2019). The Response of Earth's Electron Radiation Belts to Geomagnetic Storms: Statistics from the Van Allen Probes Era Including Effects from Different Storm Drivers. *J. Geophys. Res. Space Phys.* 124, 1013–1034. doi:10.1029/2018ja026066

Turner, D. L., O'Brien, T. P., Fennell, J. F., Claudepierre, S. G., Blake, J. B., Kilpua, E. K. J., et al. (2015b). The Effects of Geomagnetic Storms on Electrons in Earth's Radiation Belts. *Geophys. Res. Lett.* 42, 9176–9184. doi:10.1002/2015gl064747

Vampola, A. (1998). "Outer Zone Energetic Electron Environment Update," in Conference on the high energy radiation background in space. Workshop record, Snowmass, CO, USA, 22-23 July 1997 (IEEE), 128–136.

Walt, M. (2005). *Introduction to Geomagnetically Trapped Radiation*. Cambridge, UK: Cambridge University Press.

West, H. I., Buck, R. M., and Walton, J. R. (1973). Electron Pitch Angle Distributions throughout the Magnetosphere as Observed on Ogo 5. *J. Geophys. Res.* 78, 1064–1081. doi:10.1029/ja078i007p01064

Zhao, H., Friedel, R., Chen, Y., Baker, D., Li, X., Malaspina, D., et al. (2021). Equatorial Pitch Angle Distributions of 1–50 keV Electrons in Earth's Inner Magnetosphere: an Empirical Model Based on the Van Allen Probes Observations. *J. Geophys. Res. Space Phys.* 126, e2020JA028322. doi:10.1029/2020ja028322

Zhao, H., Friedel, R. H. W., Chen, Y., Reeves, G. D., Baker, D. N., Li, X., et al. (2018). An Empirical Model of Radiation Belt Electron Pitch Angle Distributions Based on Van Allen Probes Measurements. *J. Geophys. Res. Space Phys.* 123, 3493–3511. doi:10.1029/2018ja025277

Zhao, X., Hao, Y., Zong, Q.-G., Zhou, X.-Z., Yue, C., Chen, X., et al. (2020). Origin of Electron Boomerang Stripes: Localized ULF Wave-Particle Interactions. *Geophys. Res. Lett.* 47, e2020GL087960. doi:10.1029/2020gl087960

Zong, Q., Rankin, R., and Zhou, X. (2017). The Interaction of Ultra-low-frequency Pc3-5 Waves with Charged Particles in Earth's Magnetosphere. *Rev. Mod. Plasma Phys.* 1, 1–90. doi:10.1007/s41614-017-0011-4

Conflict of Interest: The authors declare that the research was conducted in the absence of any commercial or financial relationships that could be construed as a potential conflict of interest.

Publisher's Note: All claims expressed in this article are solely those of the authors and do not necessarily represent those of their affiliated organizations, or those of the publisher, the editors and the reviewers. Any product that may be evaluated in this article, or claim that may be made by its manufacturer, is not guaranteed or endorsed by the publisher.